Inorganic Chemistry

pubs.acs.org/IC

Article

Complex Magnetic Order in Topochemically Reduced Rh(I)/Rh(III) $LaM_{0.5}Rh_{0.5}O_{2.25}$ (M = Co, Ni) Phases

Zheying Xu, Pardeep K. Thakur, Tien-Lin Lee, Anna Regoutz, Emmanuelle Suard, Inés Puente-Orench, and Michael A. Hayward*

Cite This: *Inorg. Chem.* 2022, 61, 15686−15692

Read Online

ACCESS | Metrics & More | Article Recommendations | Supporting Information

ABSTRACT: Topochemical reduction of the cation-disordered perovskite oxides $LaCo_{0.5}Rh_{0.5}O_3$ and $LaNi_{0.5}Rh_{0.5}O_3$ with Zr yields the partially anion-vacancy ordered phases $LaCo_{0.5}Rh_{0.5}O_{2.25}$ and $LaNi_{0.5}Rh_{0.5}O_{2.25}$, respectively. Neutron diffraction and Hard X-ray photoelectron spectroscopy (HAXPES) measurements reveal that the anion-deficient phases contain Co^{1+}/Ni^{1+} and a 1:1 mixture of Rh^{1+} and Rh^{3+} cations within a disordered array of apex-linked MO_4 square-planar and MO_5 square-based pyramidal coordination sites. Neutron diffraction data indicate that $LaCo_{0.5}Rh_{0.5}O_{2.25}$ adopts a complex antiferromagnetic ground state, which is the sum of a C-type ordering (mM_5^+) of the *xy*-components of the Co spins and a G-type ordering ($m\Gamma_1^+$) of the *z*-components of the Co spins. On warming above 75 K, the magnitude of the $m\Gamma_1^+$ component declines, attaining a zero value by 125 K, with the magnitude of the mM_5^+ component remaining unchanged up to 175 K. This magnetic behavior is rationalized on the basis of the differing d-orbital fillings of the Co^{1+} cations in MO_4 square-planar and MO_5 square-based pyramidal coordination sites. $LaNi_{0.5}Rh_{0.5}O_{2.25}$ shows no sign of long-range magnetic order at 2 K − behavior that can also be explained on the basis of the d-orbital occupation of the Ni^{1+} centers.

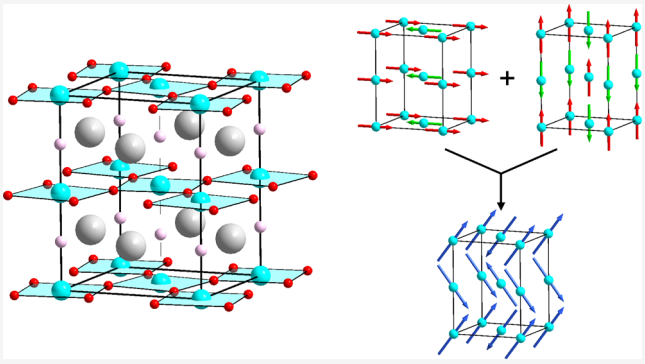

INTRODUCTION

The wide range of both chemical and physical behaviors exhibited by transition metal oxides has led to extensive and enduring interest in the chemistry and physics of these compounds. A particular attraction of many transition-metal oxide systems is that their physical and chemical behavior can be rationally tuned by modifying the configuration of the metal d-states (electron count, orbital occupation) via chemical substitution or structural modification. However, most transition metals only exhibit a limited range of thermodynamically stable oxidation-state/coordination-geometry combinations in oxide environments, limiting this approach. For example, late 4d and 5d transition metals (Ru, Rh, Re, Os, Ir) strongly disfavor low oxidation states (e.g., M^{1+} or M^{2+}) when located in extended oxide frameworks.[1] The thermodynamic instability of these low oxidation states can be attributed to the high atomization energies of the elements and relatively low cumulative ionization energies of higher-oxidation states (M^{n+} $n \geq 3$), which combine to make the M^{2+} oxidation state unstable with respect to disproportionation when bonded to good ligands such as oxide ions. This effect can be illustrated by comparing the stable binary oxides of the late 4d/5d transition metals, which have the lowest oxygen content, with their 3d transition metal analogues: RuO_2 and OsO_2 compared to FeO; Rh_2O_3 and IrO_2 compared to CoO.[1]

Topochemical reduction by anion deintercalation allows the preparation of metastable phases containing late 4d/5d transition metal cations with divalent charges, such as Ru^{2+} and Ir^{2+},[2−6] enabling their electronic and magnetic behaviors to be studied. Recently, when trying to extend this chemistry to rhodium via the preparation of the Rh^{2+}-containing extended oxides $LaSrCo_{0.5}Rh_{0.5}O_{3.25}$ and $LaSrNi_{0.5}Rh_{0.5}O_{3.25}$, we observed a further valence instability in which d^7 Rh^{2+} disproportionates into d^8 Rh^{1+} and d^6 Rh^{3+}, driven by the presence of square planar and square-based pyramidal coordination sites.[7] This behavior is analogous to the disproportionation of d^7 Pd^{3+} in KPd_2O_3 (better thought of as $K_2Pd_3^{II}Pd^{IV}O_6$)[8] or d^7 Pt^{3+} in $CdPt_3O_6$ (better thought of as $CdPt^{II}Pt_2^{IV}O_6$),[9] and in the case of the $LaSrM_{0.5}Rh_{0.5}O_{4-x}$ reduced phases, it appears to preferentially "select" the composition of the anion-deficient phases. To further explore this behavior, we have investigated the topochemical reduction

Received: August 1, 2022
Published: September 21, 2022

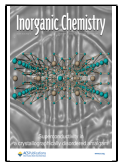

ACS Publications

© 2022 The Authors. Published by American Chemical Society

https://doi.org/10.1021/acs.inorgchem.2c02747
Inorg. Chem. 2022, 61, 15686−15692

of the analogous perovskite oxides, $LaCo_{0.5}Rh_{0.5}O_3$ and $LaNi_{0.5}Rh_{0.5}O_3$, which we report here.

EXPERIMENTAL SECTION

Preparation of $LaM_{0.5}Rh_{0.5}O_3$ (M = Co, Ni). Samples of $LaM_{0.5}Rh_{0.5}O_3$ (M = Co, Ni) were prepared by a ceramic method. Suitable quantities of La_2O_3 (99.999%, dried at 900 °C), Rh_2O_3 (99.998%, dried at 850 °C), Co_3O_4 (99.99%), or elemental Ni (99.996%) were ground together using an agate pestle and mortar. The mixed powders were heated in air at a rate of 5 °C min^{-1} to 1000 °C in alumina crucibles to oxidize the metals. After heating, the powders were pressed into pellets and then heated in air for 48 h periods at 1000, 1200, and then 1250 °C. X-ray powder diffraction data collected from the rhodium-containing perovskite phases yielded lattice parameters in agreement with previously reported literature values, as detailed in the Supporting Information.[10,11]

Reduction of $LaM_{0.5}Rh_{0.5}O_3$ (M = Co, Ni). Samples of $LaM_{0.5}Rh_{0.5}O_3$ (M = Co, Ni) were reduced using a zirconium getter.[12] Samples to be reduced were sealed in evacuated silica ampoules along with a glass "thimble" containing 2 mole equivalents of powdered zirconium, such that the two powders shared an atmosphere but were not in physical contact. Small-scale test reactions were performed in which ∼200 mg of the rhodium perovskite samples were heated at a rate of 1 °C min^{-1} to temperatures in the range 350−500 °C and held there for 3 periods of 5 days to assess reactivity. This revealed that the optimum temperatures for reduction are $LaCo_{0.5}Rh_{0.5}O_3$: 400 °C and $LaNi_{0.5}Rh_{0.5}O_3$: 420 °C. Samples of $LaCo_{0.5}Rh_{0.5}O_{3-x}$ and $LaNi_{0.5}Rh_{0.5}O_{3-x}$ studied by neutron diffraction were prepared by heating ∼2g of the corresponding oxide with 2 mole equivalents of Zr at the optimum reduction temperature for 3 periods of 5 days, with samples being reground and the Zr replaced between heating periods.

Characterization. Reaction progress and initial structural characterization were performed using laboratory X-ray powder diffraction (PXRD) data collected using a PANalytical X′pert diffractometer incorporating an X′celerator position-sensitive detector (monochromatic Cu Kα1 radiation). High-resolution synchrotron X-ray powder diffraction (SXRD) data were collected using the I11 instrument at the Diamond Light Source Ltd. Diffraction patterns were collected using Si-calibrated X-rays with an approximate wavelength of 0.825 Å from samples, sealed in 0.3 mm diameter borosilicate glass capillaries. Neutron powder diffraction (NPD) data were collected at room temperature using the D2B diffractometer (λ = 1.594 Å), and data at low temperature were collected using the D1B diffractometer (λ = 2.52 Å) at the ILL neutron source, from samples contained within vanadium cans sealed under an inert atmosphere. Rietveld refinement of powder diffraction data was performed using TOPAS Academic (V6).[13]

Thermogravimetric analysis (TGA) measurements were performed by heating powder samples at a rate of 5 °C min^{-1} under flowing 10% H_2/90%N_2, using a Mettler-Toledo MX1 thermogravimetric microbalance, and then cooling to 25 °C. DC magnetization data were collected using a Quantum Design MPMS SQUID magnetometer from samples contained in gelatin capsules.

Hard X-ray photoelectron spectroscopy (HAXPES) measurements were conducted at beamline I09 of the Diamond Light Source, UK.[14] A photon energy of 5.9 keV was selected using a double-crystal Si (111) monochromator in combination with a Si (004) channel-cut crystal post-monochromator. The end station of the beamline is equipped with a Scienta Omicron EW4000 hemispherical analyzer with a ±28° acceptance angle. All spectra were collected in grazing incidence and near-normal emission, and the sample was mounted on conducting carbon tape.

RESULTS AND DISCUSSION

Chemical and Structural Characterization of $LaM_{0.5}Rh_{0.5}O_{3-x}$ (M = Co, Ni). Heating $LaM_{0.5}Rh_{0.5}O_{3-x}$ reduced samples under a 10%H_2:90%N_2 atmosphere led to decomposition to the corresponding mixtures of La_2O_3, Rh, and Co or Ni. TGA data collected during this process indicated mass losses consistent with compositions of $LaCo_{0.5}Rh_{0.5}O_{2.25(1)}$ and $LaNi_{0.5}Rh_{0.5}O_{2.25(1)}$, as described in detail in the Supporting Information.

NPD data collected from $LaCo_{0.5}Rh_{0.5}O_{2.25}$ at room temperature could be indexed using a body-centered unit cell (a = 5.6492(2) Å, c = 7.3374(7) Å) with reflection conditions consistent with the $I4/mcm$ (#140) space group. A structural model was constructed based on a Co/Rh, B-site disordered perovskite phase with an $a^0a^0c^-$ tilting distortion, analogous to the reported structure of $SrTi_{0.5}Zr_{0.5}O_3$.[15] This model was refined against the NPD data. During the refinement, the occupancies of the oxide ion sites were allowed to vary, and it was observed that the 8h site remained fully occupied within error, but the occupancy of the 4a site declined to 0.25(1) consistent with the composition of the phase determined from TGA data. All other atomic positional and displacement parameters were allowed to vary, yielding a model that gave a good fit to the NPD data as shown in Figure 1 and detailed in Table S1, with selected bond lengths and angles in Table S3 in the Supporting Information.

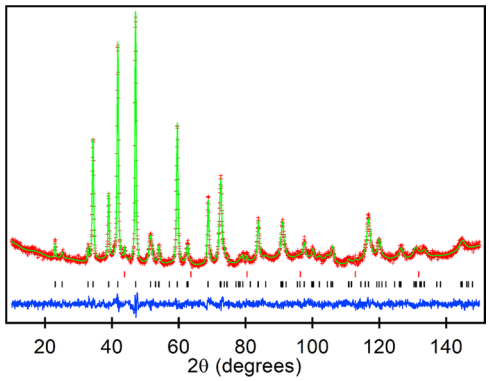

Figure 1. Observed, calculated, and difference plots from the structural refinement of $LaCo_{0.5}Rh_{0.5}O_{2.25}$ against NPD data collected at room temperature using instrument D2B. Black and red tick marks indicate peak positions for the majority phase and contributions from the vanadium sample holder, respectively.

NPD data collected from $LaNi_{0.5}Rh_{0.5}O_{2.25}$ at room temperature could also be indexed using a body-centered tetragonal unit cell (a = 5.6407(1) Å, c = 7.1794(7) Å) with reflection conditions consistent with the $I4/mcm$ (#140) space group. A structural model analogous to that used for $LaCo_{0.5}Rh_{0.5}O_{2.25}$ was refined against these data. Refinement of the anion site occupancies revealed that the 8h sites remained fully occupied, while the 4a sites yielded an occupancy of 0.24(2), consistent with the composition determined by TGA. Close inspection of the NPD data collected from $LaNi_{0.5}Rh_{0.5}O_{2.25}$ revealed additional diffraction peaks not indexed by the body-centered tetragonal cell, but which could be modeled using a second perovskite phase corresponding to 9.2 wt % unreduced $LaNi_{0.5}Rh_{0.5}O_3$. This two-phase model gave a good fit to the NPD data as shown in Figure 2 and detailed in Table S2, with selected bond lengths and angles in Table S3 in the Supporting Information.

The anion-deficient perovskite structures adopted by $LaCo_{0.5}Rh_{0.5}O_{2.25}$ and $LaNi_{0.5}Co_{0.5}O_{2.25}$ are shown in Figure 3. Topochemical reduction with Zr has removed 75% of the

https://doi.org/10.1021/acs.inorgchem.2c02747
Inorg. Chem. 2022, 61, 15686−15692

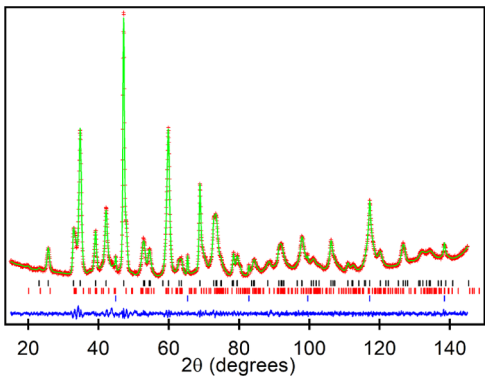

Figure 2. Observed, calculated, and difference plots from the structural refinement of $LaNi_{0.5}Rh_{0.5}O_{2.25}$ against NPD data collected at room temperature using instrument D2B. Black and red and blue tick marks indicate peak positions for the majority phase and a $LaNi_{0.5}Rh_{0.5}O_3$ secondary phase and contributions from the vanadium sample holder, respectively.

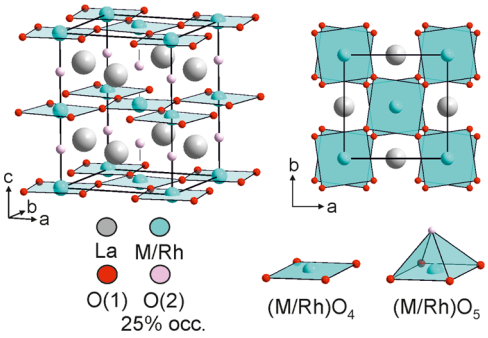

Figure 3. Structure of $LaM_{0.5}Rh_{0.5}O_{2.25}$ (M = Co, Ni) and the local $(M/Rh)O_x$ coordination polyhedra.

O(2) apical oxide ions from the parent $LaM_{0.5}Rh_{0.5}O_3$ phases to yield materials in which the apex-linked $(M/Rh)O_6$ units have been converted into a 1:1 disordered array of $(M/Rh)O_4$ square planes and $(M/Rh)O_5$ square-based pyramids, as shown in Figure 3. Thus, it can be seen that the topochemical reduction of $LaM_{0.5}Rh_{0.5}O_3$ (M = Co, Ni) phases to $LaM_{0.5}Rh_{0.5}O_{2.25}$ phases is structurally analogous to the reduction of $LaSrM_{0.5}Rh_{0.5}O_4$ n = 1 Ruddlesden−Popper phases to $LaSrM_{0.5}Rh_{0.5}O_{3.25}$ phases, as these latter reduced phases also contain disordered arrays of $(M/Rh)O_4$ square planes and $(M/Rh)O_5$ square-based pyramids.[7] Indeed, comparison of the bond lengths of the $LaM_{0.5}Rh_{0.5}O_{2.25}$ phases (Table S3) with those of the $LaSrM_{0.5}Rh_{0.5}O_{3.25}$ materials reveals that the transition-metal coordination environments in corresponding phases are remarkably similar (<(Rh/Co)-O_{eq}> = 2.065 Å, <(Rh/Co)-O_{ax}> = 1.802 Å; <(Rh/Ni)-O_{eq}> = 2.059 Å, <(Rh/Ni)-O_{ax}> = 1.790 Å),[7] suggesting that the corresponding reduced phases have the same combination of average transition-metal oxidations states: Co^{1+}/Ni^{1+} (seen previously in a number of topochemically reduced phases)[3,4,6,16−18] combined with "Rh^{2+}."

Given that the nominal Rh^{2+} centers in $LaSrCo_{0.5}Rh_{0.5}O_{3.25}$ and $LaSrNi_{0.5}Rh_{0.5}O_{3.25}$ are observed to disproportionate into Rh^{1+} and Rh^{3+}, driven by the presence of square-planar and square-pyramidal coordination sites, it appeared likely that the nominal Rh^{2+} centers in the $LaM_{0.5}Rh_{0.5}O_{2.25}$ phases would also undergo a similar disproportionation. To investigate this possibility, HAXPES was used to explore the chemical state of the $LaCo_{0.5}Rh_{0.5}O_{2.25}$ sample. The survey spectrum (Figure S5 in the Supporting Information) showed all expected core-level features as well as a small contribution from adventitious carbon. The main La 3d and Co 2p core-level spectra (Figure 4a) are commensurate with the oxide environments present in

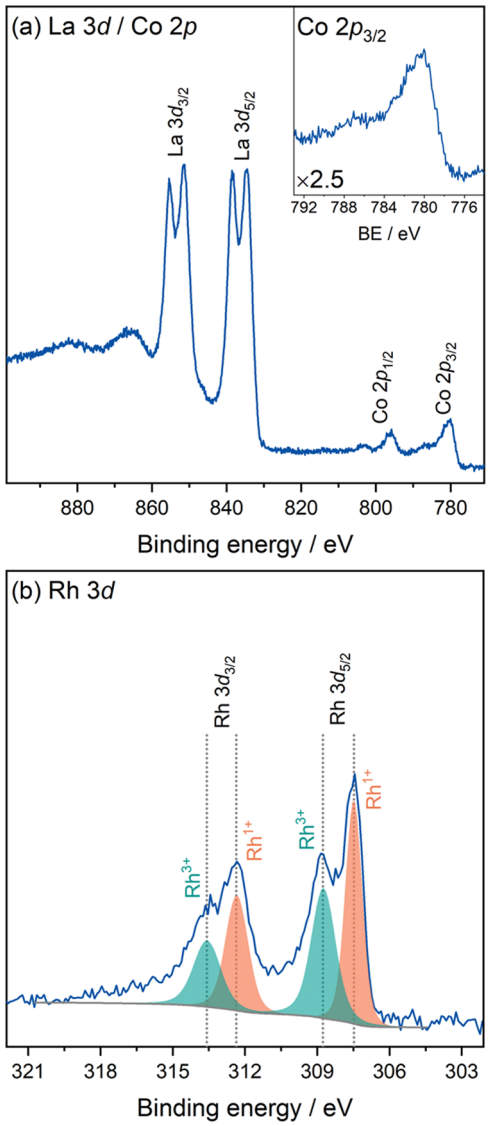

Figure 4. HAXPES core-level spectra of $LaCo_{0.5}Rh_{0.5}O_{2.25}$, including (a) La 3d/Co 2p and (b) Rh 3d. The inset in panel (a) shows a magnified (×2.5) view of the Co $2p_{3/2}$ line.

$LaCo_{0.5}Rh_{0.5}O_{2.25}$. The Rh 3d core level (Figure 4b) confirms the disproportionation of Rh^{2+} centers, showing a clear split into a lower binding energy (BE) Rh^{1+} (at 307.5 and 312.4 eV) and a higher BE Rh^{3+} component (at 308.8 and 313.6 eV) for both the Rh $3d_{5/2}$ and $3d_{3/2}$ components. The main advantage of using HAXPES instead of conventional soft X-ray photoelectron spectroscopy (SXPS) is the increase in probing depth and therefore the bulk sensitivity of the measurements, excluding that this is purely a surface effect.[19] The O 1s spectrum (Figure S5 in the Supporting Information) emphasizes the probing depth with only a low contribution from surface hydroxide species, in particular, for a powder mixed oxide sample. Although the peak fit of the Rh 3d core level is complicated due to the complex background displayed,

https://doi.org/10.1021/acs.inorgchem.2c02747
Inorg. Chem. 2022, 61, 15686−15692

fits of the Rh^{1+} and Rh^{3+} components result in line shapes matching previous observations for related oxides, including a slight increase in peak width for the $3d_{3/2}$ component from Coster–Kronig broadening.[7,20,21] Voigt functions were used for all fitted peaks with the Gaussian and Lorentzian contributions allowed to vary between 20 and 30% as the tails are not well defined due to the complex background. The full width at half-maximum (FWHM) for the Rh^{1+} component in the Rh 3d spectrum is 0.8 eV for $3d_{5/2}$ and 1.1 eV for $3d_{3/2}$, with an area ratio of 3.0:2.1. Based on the areas resulting from the peak fit, an approximate 1:1 ratio of the Rh^{1+} and Rh^{3+} states is observed. The presence of Rh^{+1} states is further corroborated by the valence spectrum (Figure S5 in the Supporting Information), which shows a clear contribution from these states just below the Fermi level (E_F).

Magnetic Characterization of $LaM_{0.5}Rh_{0.5}O_{3-x}$ (M = Co, Ni). Magnetization data collected from $LaCo_{0.5}Rh_{0.5}O_{2.25}$ and $LaNi_{0.5}Rh_{0.5}O_{2.25}$ indicate that the samples prepared of these materials contain small amounts of ferromagnetic Co and Ni, respectively. Thus, magnetization data were collected using a "ferromagnetic subtraction" technique, described in detail in the Supporting Information, which utilizes the observation that the magnetization of Co and Ni saturate in applied fields greater than 2T.

The paramagnetic susceptibility of $LaNi_{0.5}Rh_{0.5}O_{2.25}$ (Figure 5) can be fit by the Curie–Weiss law ($\chi = C/(T-\theta)$) in the temperature range $70 < T/K < 300$ to yield values of C = 0.116(2) cm^3 K mol^{-1} and $\theta = -9.21$ K. The observed value of the Curie constant is broadly consistent with the value expected for a combination of $S = 1/2$ Ni^{1+} and $S = 0$, $Rh^{1+}/S = 0$, Rh^{3+} ($C_{expected}$ = 0.1875 cm^3 K mol^{-1}). Below 70 K, the paramagnetic susceptibility deviates from the Curie–Weiss law and there is a sharp increase in the saturated ferromagnetic moment of the sample, suggesting the onset of magnetic order. However, neutron powder diffraction data collected from $LaNi_{0.5}Rh_{0.5}O_{2.25}$ at 2 K show no evidence of long-range magnetic order, as shown in Figure S7 in the Supporting Information.

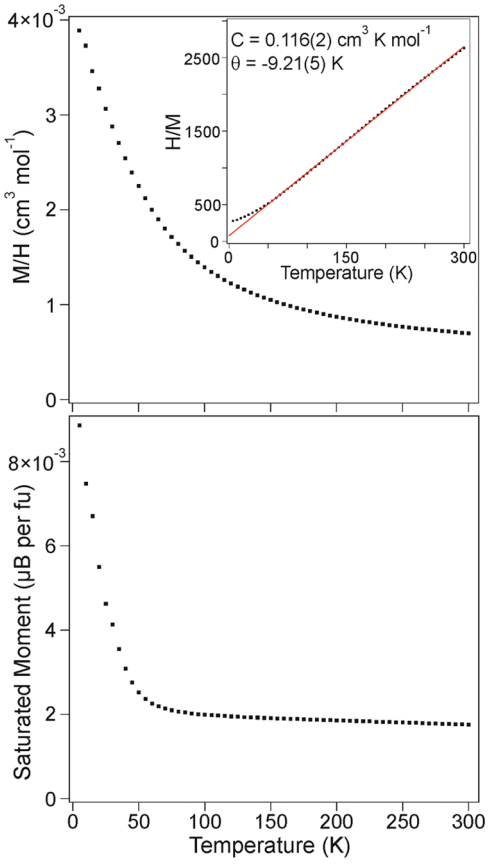

Figure 5. Paramagnetic susceptibility (top) and saturated ferromagnetic moment (bottom) of $LaNi_{0.5}Rh_{0.5}O_{2.25}$ plotted as a function of temperature. The inset shows fit to the Curie–Weiss law in the range $70 < T/K < 300$.

The magnetic behavior of $LaCo_{0.5}Rh_{0.5}O_{2.25}$ is more complex. The paramagnetic susceptibility of $LaCo_{0.5}Rh_{0.5}O_{2.25}$ (Figure 6) follows the mathematical form of the Curie–Weiss law ($\chi = C/(T-\theta)$) in the range $210 < T/K < 300$, as shown in Figure S8 in the Supporting information. However, the parameters extracted by fitting the data (C = 1.77 cm^3 K mol^{-1}, $\theta = -292$ K) are much larger than would be expected from a combination of $S = 1$ Co^{1+} centers and $S = 0$, $Rh^{1+}/S = 0$, Rh^{3+} centers ($C_{expected}$ = 0.5 cm^3 K mol^{-1}), indicating that a "simple paramagnetic" description is not valid for $LaCo_{0.5}Rh_{0.5}O_{2.25}$ in this temperature range. On cooling, the magnetic susceptibility of $LaCo_{0.5}Rh_{0.5}O_{2.25}$ exhibits a weak

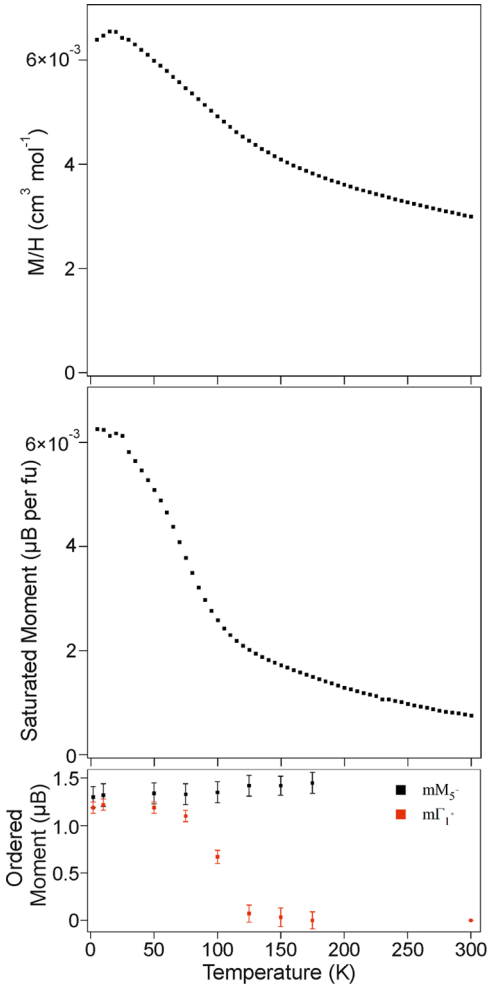

Figure 6. Paramagnetic susceptibility (top) and saturated ferromagnetic moment (middle) of $LaCo_{0.5}Rh_{0.5}O_{2.25}$ plotted as a function of temperature. Ordered magnetic moment (bottom) extracted from fits to NPD data.

https://doi.org/10.1021/acs.inorgchem.2c02747
Inorg. Chem. 2022, 61, 15686−15692

maximum at $T \sim 15$ K, and the saturated ferromagnetic moment of the sample shows a sharp increase below 125 K, suggesting a transition to a magnetically ordered state. Magnetization-field isotherms collected from $LaCo_{0.5}Rh_{0.5}O_{2.25}$ at 5 K after cooling from 300 K in an applied field of 50,000 Oe (Figure S9) show weak hysteresis and are displaced from the origin, indicating a glassy component to the magnetic state below 30 K.

Neutron diffraction data collected from $LaCo_{0.5}Rh_{0.5}O_{2.25}$ at 2 K exhibit magnetic Bragg scattering which can be indexed using a cell of the same dimensions as the crystallographic cell. Symmetry analysis reveals that there are six symmetry-distinct magnetic models which are compatible with the cell and the *I*4/*mcm* crystallographic symmetry of the phase.[22,23] Simulating the neutron scattering from these magnetic models revealed that no single model can account for all of the observed magnetic scattering in the NPD data. A magnetic model corresponding to a C-type ordering of moments aligned in the *xy*-plane (transforming as the mM_5^+ irreducible representation of *I*4/*mcm*, described in magnetic space group 60.388), shown in Figure 7, accounts for all of the observed peaks except the $[101]_m$ reflection (d = 4.47 Å). However, a G-type ordering of spins aligned along the *z*-axis (transforming as the $m\Gamma_1^+$ irreducible representation of *I*4/*mcm*, described in magnetic space group 140.541), shown in Figure 7, can account for the observed intensity of the $[101]_m$ Bragg peak, so a magnetic model consisting of a combination of the mM_5^+ and $m\Gamma_1^+$ orderings was refined against the NPD data, in addition to a crystallographic model. During the refinement, it was assumed that only cobalt contributed to the magnetic behavior of $LaCo_{0.5}Rh_{0.5}O_{2.25}$, due to the expected diamagnetism of the Rh^{1+}/Rh^{3+} centers. The combined model achieved a good fit to the data collected at 2 K, as shown in Figure 7 and described in Table S7, to yield ordered moments of 1.30(11) μB and 1.19(6) μB for the mM_5^+ and $m\Gamma_1^+$ components, respectively, and a total moment of 1.76 μB for each cobalt ion.

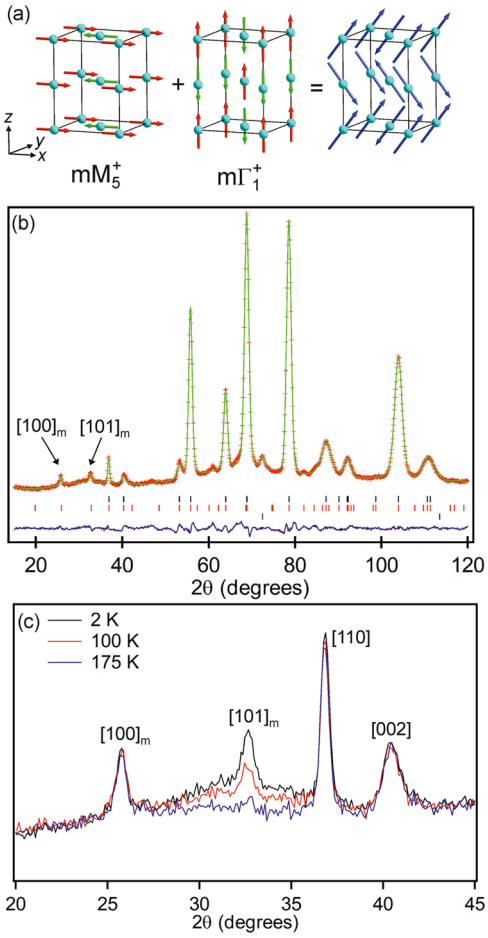

Figure 7. (a) mM_5^+ and $m\Gamma_1^+$ symmetry magnetic orderings on $LaCo_{0.5}Rh_{0.5}O_{2.25}$. (b) Observed, calculated, and difference plots from a combined magnetic and structural refinement of $LaCo_{0.5}Rh_{0.5}O_{2.25}$ against NPD data collected at 2 K using instrument D1B. Black ticks indicate peak positions for the crystallographic cell, red ticks the magnetic cell, and blue ticks contributions from the vanadium sample holder. (c) A selected region of NPD data collected from $LaCo_{0.5}Rh_{0.5}O_{2.25}$ at 2, 100, and 175 K.

On warming, the intensity of the $[101]_m$ Bragg reflection declines in data sets collected at temperatures above 75 K, while the remaining magnetic Bragg peaks retained their intensities, as shown in Figure 7. Fitting these NPD data to the two-component magnetic model reveals that the ordered moment of the $m\Gamma_1^+$ component declines to zero between 75 and 125 K, while the ordered moment of the mM_5^+ component remains unchanged within error up to 175 K, as shown in Figure 6. Close inspection of the NPD data further revealed that the $[101]_m$ Bragg peak sits on top of a broad diffuse feature, centered at the same *d*-spacing, and that the intensity of this diffuse feature declines with the intensity of the $[101]_m$ reflection. Unfortunately, we were unable to measure NPD data between 175 and 300 K for operational reasons, so we could not observe the decline of the magnetic scattering intensity from the mM_5^+ component.

The magnetic behavior of $LaCo_{0.5}Rh_{0.5}O_{2.25}$ can be rationalized by considering the magnetic coupling interactions, which exist between the S = 1, Co^{1+} cations (interactions with the S = 0, Rh^{1+} and Rh^{3+} are considered too weak to be relevant in this analysis). These Co−Co couplings can be separated into two types: intralayer couplings within the $Co_{0.5}Rh_{0.5}O_2$ planes (i.e., the *xy*-plane of the material) and interlayer couplings between the Co^{1+} cations in adjacent $Co_{0.5}Rh_{0.5}O_2$ layers (i.e., couplings along the *z*-axis). Considering the in-plane interactions first, there are three different couplings to consider between C_{4v} and D_{4h} coordinated Co^{1+} centers: C_{4v}−C_{4v}, C_{4v}−D_{4h}, and D_{4h}−D_{4h}. As shown in Figure 8, the in-plane magnetic couplings are dominated by the $(3d_{x^2-y^2})^1$−O2p−$(3d_{x^2-y^2})^1$ σ-type superexchange interaction, which is strongly antiferromagnetic, with only weak contributions from the π-symmetry $(3d_{xy})$−O2p−$(3d_{xy})$ couplings. The resultant strong, in-plane antiferromagnetic coupling is consistent with the in-plane antiferromagnetic orderings present in both the mM_5^+ and $m\Gamma_1^+$ irreducibles.

There are also three interlayer couplings: C_{4v}−C_{4v} (direct and super exchange), D_{4h}−C_{4v} (direct exchange), and D_{4h}−D_{4h} (direct exchange). As shown in Figure 8, when S = 1 Co^{1+} cations reside in D_{4h} coordination, all of the d-orbitals with a *z*-component are filled, so the D_{4h}−D_{4h} interlayer coupling will be negligible. In contrast, the C_{4v}−C_{4v} interaction will either be a strong $(3d_{z^2})^1$−O2p_z−$(3d_{z^2})^1$ superexchange if the centers are linked by an oxide ion or $(3d_{z^2})^1$−$(3d_{z^2})^1$ direct exchange if the centers are not linked by an oxide ion. Both of these couplings are strongly antiferromagnetic, so the C_{4v}−C_{4v} interlayer interaction is consistent with the $m\Gamma_1^+$ irreducible (G-type antiferromagnetic order). In contrast, the C_{4v}−D_{4h} coupling is a $(3d_{z^2})^1$−$(3d_{z^2})^2$ direct exchange interaction that is

https://doi.org/10.1021/acs.inorgchem.2c02747
Inorg. Chem. 2022, 61, 15686−15692

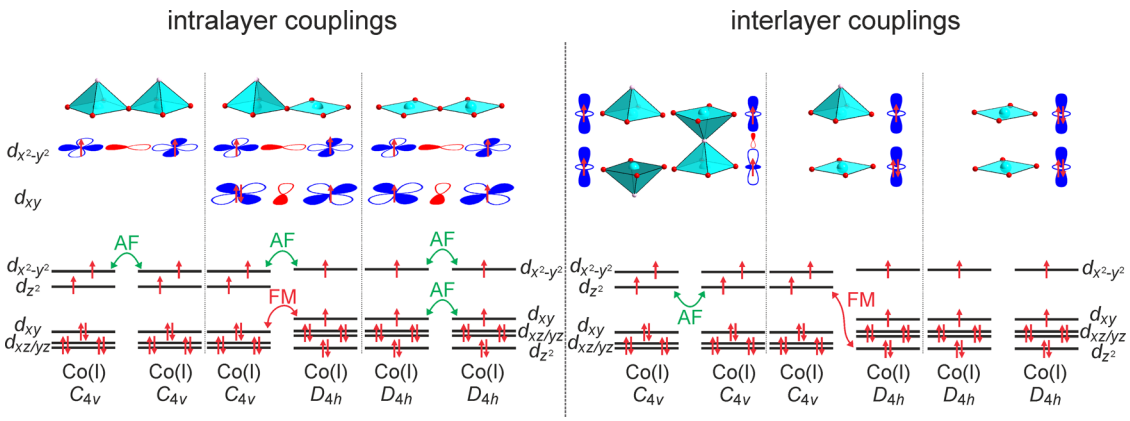

Figure 8. Intralayer and interlayer magnetic couplings present in $LaCo_{0.5}Rh_{0.5}O_{2.25}$.

ferromagnetic, as shown in Figure 8. Thus, the C_{4v}–D_{4h} interlayer coupling is consistent with the mM_5^+ irreducible (C-type antiferromagnetic order). In a 1:1 disordered array of C_{4v} and D_{4h} centers, there will be twice as many C_{4v}–D_{4h} interlayer couplings as C_{4v}–C_{4v}, consistent with the persistence of the mM_5^+ ordering to a higher temperature than the $m\Gamma_1^+$ ordering.

We, therefore, propose a model in which the interlayer and intralayer couplings between the C_{4v} and D_{4h} coordinated cobalt centers combine at 2 K to yield the mM_5^+ + $m\Gamma_1^+$ ordered model shown in Figure 7a. On warming above 75 K, the magnitude of the $m\Gamma_1^+$ ordered component diminishes, achieving a zero value by T = 125 K. On further warming, the magnitude of mM_5^+ component remains constant, within error up to 175 K. The lack of NPD data between 175 and 300 K makes it impossible to definitively determine the Néel temperature of the mM_5^+ component, but we know that there is no 3D long-range magnetic order at 300 K from the NPD data collected using the D2B instrument. It seems likely that the second magnetic transition occurs at around 200 K, the temperature at which the reciprocal of the magnetic susceptibility of the phase stops being linear with temperature. The large, nonphysical Curie constant extracted from the susceptibility data of $LaCo_{0.5}Rh_{0.5}O_{2.25}$ suggests that strong, in-plane 2D magnetic correlations persist to temperatures above 300 K and further suggests that the magnetic transition associated with the loss of the magnetic scattering from the mM_5^+ component may be better described as a 3D-to-2D transition, hence its weak signature in the magnetic susceptibility data.

A magnetic ordering scheme arising from the addition of opposed coupling interactions (the ferromagnetic and antiferromagnetic interlayer couplings in the mM_5^+ and $m\Gamma_1^+$ components, respectively) is unusual. Typically, such opposed coupling interactions would be expected to frustrate each other leading to spin-glass behavior. In this instance, we believe that the dilution of the magnetic lattice by diamagnetic Rh^{1+} and Rh^{3+} centers gives the system enough flexibility to relieve this frustration, enabling the mM_5^+ and $m\Gamma_1^+$ components to coexist and order the *xy*- and *z*-components of the magnetic moments, respectively. As noted above, a significant amount of diffuse scattering can be observed under the $[110]_m$ reflection (Figure 7), indicating that the $m\Gamma_1^+$ component of the magnetic order is short ranged in parts of the sample, while the displacement of the field-cooled magnetization-field isotherms, observed below 30 K, indicates a glassy component to the magnetic behavior; both features suggest that the competition/frustration between the interlayer ferromagnetic and antiferromagnetic couplings is not completely lifted.

Using the same analysis strategy, the lack of long-range magnetic order in $LaNi_{0.5}Rh_{0.5}O_{2.25}$ can be rationalized by noting that the additional electron present in d^9 Ni^{1+}, compared to d^8 Co^{1+}, will fill the $3d_{z^2}$ orbital for the C_{4v}-coordinated Ni^{1+} and the $3d_{xy}$ orbital for the D_{4h}-coordinated Ni^{1+} centers. As a result, all of the orbitals with a component parallel to the *z*-axis are filled, so while we would expect strong intralayer antiferromagnetic couplings in $LaNi_{0.5}Rh_{0.5}O_{2.25}$, the interlayer couplings will be extremely weak, explaining the lack of long-range magnetic order in this phase.

■ CONCLUSIONS

Topochemical reduction of the cation-disordered perovskite oxides $LaCo_{0.5}Rh_{0.5}O_3$ and $LaNi_{0.5}Rh_{0.5}O_3$ yields $LaCo_{0.5}Rh_{0.5}O_{2.25}$ and $LaNi_{0.5}Rh_{0.5}O_{2.25}$, respectively – compositions that appear to be selected by the stabilization provided by Rh^{1+} and Rh^{3+} centers located in square-planar and square-based pyramidal coordination sites, respectively.

The resulting arrays of Co^{1+}, diluted in the perovskite framework by diamagnetic Rh^{1+}/Rh^{3+} in $LaCo_{0.5}Rh_{0.5}O_{2.25}$, exhibit complex magnetic order, arising from the differing d-orbital occupations of the D_{4h} square-planar and C_{4v} square-pyramidal coordinated Co^{1+} centers. These differing local electronic configurations mean that the C_{4v}–C_{4v} interlayer coupling is antiferromagnetic, while the corresponding D_{4h}–C_{4v} coupling is ferromagnetic. Unusually, the competition between these opposed interlayer magnetic couplings leads to a sequential ordering of the in-plane *xy* and interlayer *z* components of the Co spins, rather than magnetic frustration and spin glass behavior.

■ ASSOCIATED CONTENT

Supporting Information

The Supporting Information is available free of charge at https://pubs.acs.org/doi/10.1021/acs.inorgchem.2c02747.

Description of the structural characterization of $LaCo_{0.5}Rh_{0.5}O_3$ and $LaNi_{0.5}Rh_{0.5}O_3$; a complete description of the chemical, structural, and magnetic characterization of $LaCo_{0.5}Rh_{0.5}O_{2.25}$ and $LaNi_{0.5}Rh_{0.5}O_{2.25}$ at 298 and 2 K (PDF)

https://doi.org/10.1021/acs.inorgchem.2c02747
Inorg. Chem. 2022, 61, 15686–15692

AUTHOR INFORMATION

Corresponding Author

Michael A. Hayward − *Department of Chemistry, University of Oxford, Inorganic Chemistry Laboratory, Oxford OX1 3QR, U.K.;* orcid.org/0000-0002-6248-2063; Email: michael.hayward@chem.ox.ac.uk

Authors

Zheying Xu − *Department of Chemistry, University of Oxford, Inorganic Chemistry Laboratory, Oxford OX1 3QR, U.K.*

Pardeep K. Thakur − *Diamond Light Source Ltd., Diamond House, Harwell Science and Innovation Campus, Didcot OX11 0DE, U.K.;* orcid.org/0000-0002-9599-0531

Tien-Lin Lee − *Diamond Light Source Ltd., Diamond House, Harwell Science and Innovation Campus, Didcot OX11 0DE, U.K.*

Anna Regoutz − *Department of Chemistry, University College London, London WC1H 0AJ, U.K.;* orcid.org/0000-0002-3747-3763

Emmanuelle Suard − *Institut Laue-Langevin - 71 avenue des Martyrs, 38000 Grenoble, France;* orcid.org/0000-0001-5966-5929

Inés Puente-Orench − *Institut Laue-Langevin - 71 avenue des Martyrs, 38000 Grenoble, France*

Complete contact information is available at: https://pubs.acs.org/10.1021/acs.inorgchem.2c02747

Author Contributions

The manuscript was written through contributions of all authors.

Notes

The authors declare no competing financial interest.

ACKNOWLEDGMENTS

SXRD measurements at the Diamond Light Source were performed as part of the Block Allocation Group award "Oxford Solid State Chemistry BAG to probe composition-structure-property relationships in solids" (CY25166). MAH thanks the EPSRC (EP/T027991/1) for funding. A.R. acknowledges support from the Analytical Chemistry Trust Fund for her CAMS-UK Fellowship. The authors acknowledge Diamond Light Source for time on Beamline I09 under Proposal NT29451-1.

REFERENCES

(1) Greenwood, N. N.; Earnshaw, A., *Chemistry of the Elements.* Pergamon Press: Oxford, 1997.

(2) Denis Romero, F.; Burr, S. J.; McGrady, J. E.; Gianolio, D.; Cibin, G.; Hayward, M. A. $SrFe_{0.5}Ru_{0.5}O_2$: sqaure-planar Ru^{2+} in an extended oxide. *J. Am. Chem. Soc.* **2013**, *135*, 1838−1844.

(3) Patino, M. A.; Zeng, D.; Bower, R.; McGrady, J. E.; Hayward, M. A. Coupled electronic and magnetic phase transition in the infinite-layer phase $LaSrNiRuO_4$. *Inorg. Chem.* **2016**, *55*, 9012−9016.

(4) Xu, Z. Y.; Jin, L.; Backhaus, J. K.; Green, F.; Hayward, M. A. Hole and Electron Doping of Topochemically Reduced Ni(I)/Ru(II) Insulating Ferromagnetic Oxides. *Inorg. Chem.* **2021**, *60*, 14904−14912.

(5) Page, J. E.; Morgan, H. W. T.; Zeng, D.; Manuel, P.; McGrady, J. E.; Hayward, M. A. Sr_2FeIrO_4: square-planar Ir(II) in an extended oxide. *Inorg. Chem.* **2018**, *57*, 13577−13585.

(6) Page, J. E.; Hayward, M. A. Structure and Magnetism of $(La/Sr)_2M_{0.5}Ir^{V0.5}O_4$ and Topochemically Reduced $(La/Sr)_2M_{0.5}I^{II0.5}O_3$ (M = Fe, Co) Complex Oxides. *Inorg. Chem.* **2019**, *58*, 6336−6343.

(7) Xu, Z.; Palgrave, R. G.; Hayward, M. A. $LaSrCo_{0.5}Rh_{0.5}O_{3.25}$ and $LaSrNi_{0.5}Rh_{0.5}O_{3.25}$: Topochemically Reduced, Mixed Valence Rh(I)/Rh(III) Oxides. *Inorg. Chem.* **2020**, *59*, 13767−13773.

(8) Panin, R. V.; Khasanova, N. R.; Bougerol, C.; Schnelle, W.; Van Tendeloo, G.; Antipov, E. V. Ordering of Pd^{2+} and Pd^{4+} in the Mixed-Valent Palladate KPd_2O_3. *Inorg. Chem.* **2010**, *49*, 1295−1297.

(9) Prewitt, C. T.; Schwartz, K. B.; Shannon, R. D. Synthesis and Structure of Orthorhombic Cadmium Platinum Oxide, $CdPt_3O_6$. *Acta Crystallogr., Sect. C: Cryst. Struct. Commun.* **1983**, *39*, 519−521.

(10) Li, J.; Smith, A. E.; Kwong, K. S.; Powell, C.; Sleight, A. W.; Subramanian, M. A. Lattice crossover and mixed valency in the $LaCo_{1-x}Rh_xO_3$ solid solution. *J. Solid State Chem.* **2010**, *183*, 1388−1393.

(11) Battle, P. D.; Vente, J. F. Structural and magnetic characterization of La_2NiRhO_6. *J. Solid State Chem.* **1999**, *146*, 163−167.

(12) Hayward, M. A. Soft chemistry synthesis of oxides. In *Comprehensive Inorganic Chemistry II*; Reedijk, J.; Poeppelmeier, K. R., Eds.; Elsevier: Oxford, 2013; Vol. *2*, pp 417−453.

(13) Coelho, A. A. *TOPAS Academic: General profile and Structure Analysis Software For Powder Diffraction Data*; Bruker AXS: Karlsruhe, Germany, 2016.

(14) Lee, T. L.; Duncan, D. A. A Two-Color Beamline for Electron Spectroscopies at Diamond Light Source. *Synchrotron Radiation News* **2018**, *31*, 16−22.

(15) Wong, T. K. Y.; Kennedy, B. J.; Howard, C. J.; Hunter, B. A.; Vogt, T. Crystal structures and phase transitions in the $SrTiO_3$-$SrZrO_3$ solid solution. *J. Solid State Chem.* **2001**, *156*, 255−263.

(16) Hayward, M. A.; Green, M. A.; Rosseinsky, M. J.; Sloan, J. Sodium hydride as a powerful reducing agent for topotactic oxide deintercalation: Synthesis and characterization of the nickel(I) oxide $LaNiO_2$. *J. Am. Chem. Soc.* **1999**, *121*, 8843−8854.

(17) Hayward, M. A.; Rosseinsky, M. J. Synthesis of the infinite layer Ni(I) phase $NdNiO_{2+x}$ by low temperature reduction of $NdNiO_3$ with sodium hydride. *Solid State Sci.* **2003**, *5*, 839−850.

(18) Seddon, J.; Suard, E.; Hayward, M. A. Topotactic reduction of $YBaCo_2O_5$ and $LaBaCo_2O_5$: square-planer Co(I) in an extended oxide. *J. Am. Chem. Soc.* **2010**, *132*, 2802−2810.

(19) Kalha, C.; Fernando, N. K.; Bhatt, P.; Johansson, F. O. L.; Lindblad, A.; Rensmo, H.; Medina, L. Z.; Lindblad, R.; Siol, S.; Jeurgens, L. P. H.; Cancellieri, C.; Rossnagel, K.; Medjanik, K.; Schonhense, G.; Simon, M.; Gray, A. X.; Nemsak, S.; Lomker, P.; Schlueter, C.; Regoutz, A. Hard x-ray photoelectron spectroscopy: a snapshot of the state-of-the-art in 2020. *J. Phys.:Condens. Matter* **2021**, *33*, No. 233001.

(20) Coster, D.; Kronig, R. D. New type of auger effect and its influence on the x-ray spectrum. *Physica* **1935**, *2*, 13−24.

(21) Kövér, L.; Tóth, J.; Itoh, A. An experimental method for resolution calibration of electron spectrometers. *Acta Phys. Hung.* **1989**, *65*, 217−223.

(22) Campbell, B. J.; Stokes, H. T.; Tanner, D. E.; Hatch, D. M. ISODISPLACE: a web-based tool for exploring structural distortions. *J. Appl. Crystallogr.* **2006**, *39*, 607−614.

(23) Stokes, H. T.; Hatch, D. M.; Campbell, B. J. *ISOTROPY Software Suite*, iso.byu.edu, 2007.